SEDIMENTOLOGY the journal of the International Association of Sedimentologists

Sedimentology (2010) **57,** 786–805 doi: 10.1111/j.1365-3091.2009.01119.x

Diagenetic formation of gypsum and dolomite in a cold-water coral mound in the Porcupine Seabight, off Ireland

HANS PIRLET*, LAURA M. WEHRMANN†,‡, BENJAMIN BRUNNER†, NORBERT FRANK§, JAN DEWANCKELE¶,**, DAVID VAN ROOIJ*, ANNELEEN FOUBERT††, RUDY SWENNEN††, LIEVEN NAUDTS*, MATTHIEU BOONE**, VEERLE CNUDDE¶,** and JEAN-PIERRE HENRIET*

**Renard Centre of Marine Geology, Department of Geology and Soil Science, Ghent University, Krijgslaan 281 s8, B-9000 Gent, Belgium (E-mail: hans.pirlet@ugent.be)*

†Biogeochemistry Research Group, Max Planck Institute for Marine Microbiology, Celsiusstrasse 1, D-28359 Bremen, Germany

‡Coral Reef Ecology Work Group, GeoBio-Center, Ludwig-Maximilians Universität, Richard-Wagner-Strasse 10, D-80333 München, Germany

§Laboratoire des Sciences du Climat et de L'Environnement (LSCE), Unité Mixte CEA/CNRS/UVSQ, Bat 12, Avenue de la Terrasse, F-91190 Gif-sur-Yvette, France

¶Department of Geology and Soil Science, Ghent University, Krijgslaan 281 s8, B-9000 Gent, Belgium

***Department of Subatomic and Radiation Physics, Ghent University, B-9000 Gent, Belgium*

††Department of Earth and Environmental Sciences, Geology, K.U. Leuven, Celestijnenlaan 200E, 3001 Heverlee, Belgium

ABSTRACT

Authigenic gypsum was found in a gravity core, retrieved from the top of Mound Perseverance, a giant cold-water coral mound in the Porcupine Basin, off Ireland. The occurrence of gypsum in such an environment is intriguing, because gypsum, a classic evaporitic mineral, is undersaturated with respect to sea water. Sedimentological, petrographic and isotopic evidence point to diagenetic formation of the gypsum, tied to oxidation of sedimentary sulphide minerals (i.e. pyrite). This oxidation is attributed to a phase of increased bottom currents which caused erosion and enhanced inflow of oxidizing fluids into the mound sediments. The oxidation of pyrite produced acidity, causing carbonate dissolution and subsequently leading to pore-water oversaturation with respect to gypsum and dolomite. Calculations based on the isotopic compositions of gypsum and pyrite reveal that between 21·6% and 28·6% of the sulphate incorporated into the gypsum derived from pyrite oxidation. The dissolution of carbonate increased the porosity in the affected sediment layer but promoted lithification of the sediments at the sediment-water interface. Thus, authigenic gypsum can serve as a signature for diagenetic oxidation events in carbonate-rich sediments. These observations demonstrate that fluid flow, steered by environmental factors, has an important effect on the diagenesis of coral mounds.

Keywords Cold-water coral, dolomite, early diagenesis, gypsum, *Lophelia*, Porcupine Seabight, sulphur isotopes.

INTRODUCTION

The occurrence of cold-water corals has been reported all along the Atlantic European margin over a wide bathymetric and hydrographical range (Freiwald & Roberts, 2005; Roberts *et al.*, 2006). The framework-building cold-water corals, *Lophelia pertusa* and *Madrepora oculata* are found in

northern Norway, where they form elongated reefs (Lindberg *et al.*, 2007; Wheeler *et al.*, 2007), to the Gulf of Cadiz where they occur in the vicinity of mud volcanoes (Foubert *et al.*, 2008). In the Porcupine Seabight, located south-west of Ireland, *Lophelia* and *Madrepora* have built mounds up to 200 m high (Henriet *et al.*, 1998; De Mol *et al.*, 2002; Huvenne *et al.*, 2002). In the latter area, the mounds occur in three well-delineated provinces (Fig. 1): (i) the Belgica Mound Province, on the eastern slope of the Porcupine Seabight; (ii) the Hovland Mound Province, on the northern slope of the basin; and (iii) the Magellan Mound Province which flanks the Hovland mounds to the north. The mounds in each of these provinces feature distinct morphologies (De Mol *et al.*, 2002; Van Rooij *et al.*, 2003).

Until now, little attention has been paid to the diagenetic processes that occur within these cold-water coral mounds (Noé *et al.*, 2006). The present paper focuses on the diagenetic changes observed within a gravity core (MD01-2459G) which was retrieved close to the top of Mound Perseverance (Magellan Mound Province, northern slope of the Porcupine Seabight). The aim of this study was to explore the process that led to the alteration of the corals and the formation of gypsum and dolomite crystals in the sediment. It is proposed that the presence of authigenic gypsum in carbonate-dominated sediments serves as an indicator for early diagenetic oxidation events.

Regional setting

Mound Perseverance is situated in the Magellan Mound Province, where more than 1000 mounds occur with a spatial density of *ca* 1 mound km^{-2} (Fig. 2) (Huvenne *et al.*, 2007). The growth of these mounds was influenced and shaped by north-south oscillating palaeocurrents. All mounds root on one seismic horizon, indicating a sudden start-up event (Huvenne *et al.*, 2007). According to the results of the Integrated Ocean Drilling Program (IODP) Expedition 307, the start-up event of Challenger Mound, located in the Belgica Mound Province, is dated at 2·7 Ma (Kano *et al.*, 2007).

In contrast to the Belgica mounds, which have a broad base, most Magellan mounds have an ovoid shape, suggesting growth in competition with concurrent sedimentation (De Mol *et al.*, 2002; Huvenne *et al.*, 2007). Nowadays, most mounds in the Magellan Mound Province are buried. Based on the coccolith assemblage and the stratigraphy of a core taken on top of one of the buried mounds, it was concluded that the mounds were buried before Marine Isotope Stage 6 (Foubert *et al.*, 2007). Unfortunately, this core

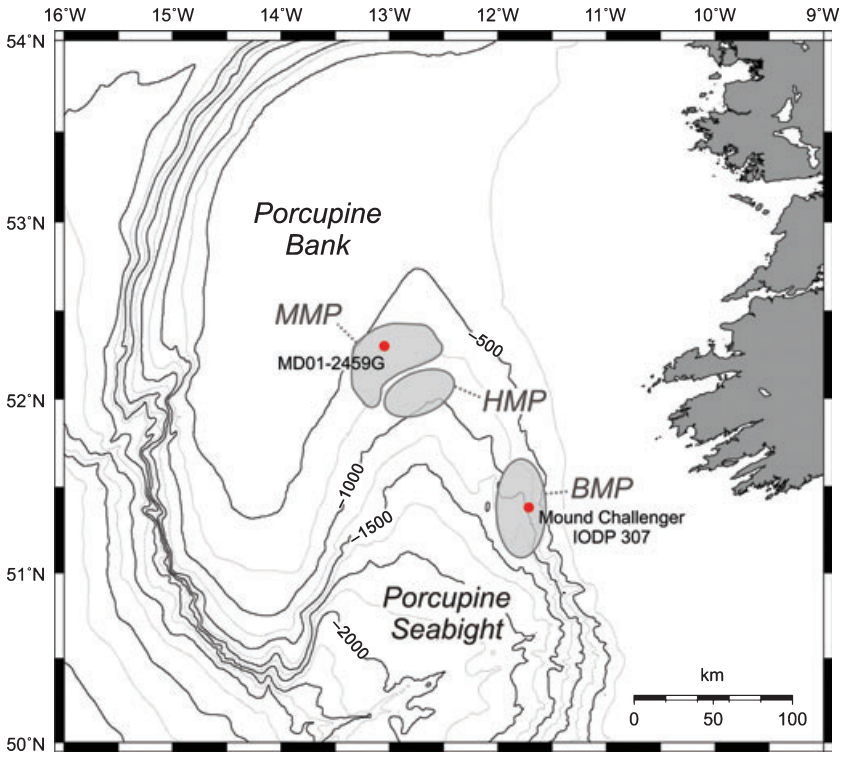

Fig. 1. Overview map of the Porcupine Seabight, south-west of Ireland, including the main morphological features and localization of core MD01-2459G. The three mound provinces: Belgica Mound Province (BMP), Hovland Mound Province (HMP) and Magellan Mound Province (MMP) are indicated.

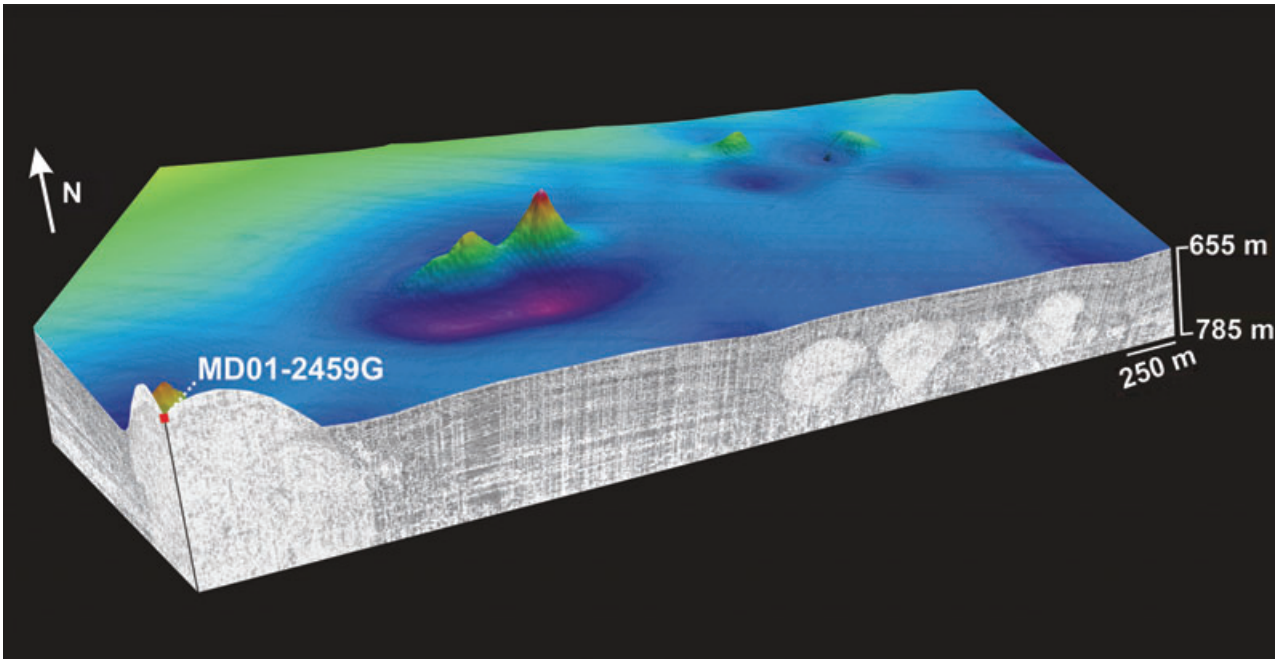

Fig. 2. Location of core MD01-2459G, close to the top of Mound Perseverance. The bathymetry, derived from 3D seismic data, is used in combination with single channel reflection seismic profiles. East of Perseverance, buried mounds are observed on the seismic line.

did not penetrate the buried mound, so the exact timing of the burial is not known. Mound Perseverance is one of few Magellan mounds which are still cropping out at the sea bed (Fig. 2). The top of this mound is situated at a water depth of 610 m and its height above the actual mound base is *ca* 160 m. The mound is elevated 50 m above the present-day sea bed and shows a NNE-SSW elongation. Video footage that was taken during the *Caracole* cruise in 2001 with *ROV Victor 6000* showed the presence of living corals on the flanks of Mound Perseverance (Huvenne *et al.*, 2007).

The water-mass stratification within the Porcupine Seabight has been reviewed by Hargreaves (1984), Rice *et al.* (1991) and White (2001). The depth range of the mounds in this area (600 to 1000 m) marks the upper boundary of the Mediterranean Outflow Water (MOW) which is overlain by the Eastern North Atlantic Water. Both water masses are carried northwards by the eastern boundary slope current (White, 2007). At the northern end of the seabight, where the Magellan mounds are located, currents are relatively weaker with some evidence of topographic steering of the mean flow cyclonically around the slope of the Porcupine Basin (White, 2001, 2007; Huvenne *et al.*, 2002).

Diagenesis in cold-water coral mounds

It is important to understand how early diagenetic processes alter the original sedimentary record of mound sediments to decipher their geological history. The imprint on the sediment thereby provides information about the microbial and geochemical processes that occur within cold-water coral mounds.

Until recently, limited attention has been paid to these diagenetic processes. The most prominent diagenetic feature in cold-water coral mounds is the dissolution of the aragonitic corals (Foubert *et al.*, 2007). The latter authors described the dissolution of coral fragments and precipitation of carbonate in mounds in the Porcupine Seabight; they attributed the coral alteration to oxidation of organic matter, affecting the saturation state of aragonite. Geochemical processes controlling the preservation of corals in cold-water coral mounds have been described in detail by Ferdelman *et al.* (2006) and Wehrmann *et al.* (2009). Both studies suggest a coupling between microbial-mediated organic matter degradation and carbonate-mineral diagenesis and link sediment composition and coral skeleton preservation by showing that the availability of reactive iron leads to an effective buffering of the pore-water carbonate system.

MATERIAL AND METHODS

Sedimentological data

Core MD01-2459G was obtained with a gravity corer during the MD123-Geosciences campaign with *R/V Marion Dufresne* in September 2001. The core was retrieved close to the top of Mound Perseverance at a water depth of 610 m with a recovery of 1079 cm (52°18′00·60″ N 13°02′51·00″ W) (Fig. 2). After retrieval, the core was analysed on board with the GEOTEK Multi Sensor Core Logger (Geotek, Daventry, UK) with a resolution of 2 cm, measuring magnetic susceptibility, gamma-ray density and P-wave velocity (Van Rooij *et al.*, 2001; Foubert *et al.*, 2007). X-ray images were obtained using the SCOPIX X-ray equipment (Département de Géologie et d'Océanographie-UMR 5805, Université Bordeaux I, France), described by (Foubert *et al.*, 2007).

The major chemical element composition was analysed using an AVAATECH XRF core scanner (AVAATECH, Den Burg, the Netherlands) installed at the Royal Netherlands Institute for Sea Research (Royal NIOZ). X-ray fluorescence is a semi-quantitative, non-destructive method which provides high-resolution records of chemical composition on split sediment cores (Richter *et al.*, 2006). The principle of X-ray fluorescence is explained in detail by Jenkins & De Vries (1970).

Element intensities were measured in two runs with a resolution of 1 cm. In the first run, element intensities were measured for the elements ranging from aluminium to cobalt using a computer controlled forced air cooled Oxford 50 watt X-ray source (Oxford Instruments X-Ray Technology Inc., Scotts Valley, CA, USA) operating at a current of 0·15 mA and 10 kV. In the second run, the element intensities for the elements ranging from zinc to zirconium were determined with the X-ray source operating at a current of 0·8 mA and 30 kV. In both runs, the count time was 30 sec (Foubert & Henriet, 2009).

The different mineralogical phases of the sediment matrix of 14 samples were identified and quantified using X-ray diffraction (XRD) at the Department of Earth and Environmental Sciences, Geology, K.U. Leuven. A representative amount of sediment was dried (around 30 g) before crushing the sample by hand and passing it through a 500 μm sieve. Subsequently, 10% ZnO was added to the sample as an internal standard and the sample was powdered in a McCrone Micronizing mill (McCrone Microscopes & Accessories, Westmont, IL, USA) using 4 ml of methanol as a lubricating agent. X-ray data were collected on a Philips PW1830 diffractometer (Bragg-Bretano geometry; PANalytical BV, Almelo, the Netherlands). An angular range of 5 to 70° 2θ was measured with a step size of 0·02° and 2 sec counting time for each step. For quantitative phase analysis, the Rietveld refinement program Topas academic was used.

Micro-computer tomography scan

Computer tomography (CT) investigates the external and internal structure of objects in three dimensions, in a non-destructive way (Kak & Slaney, 1988). These CT scans were carried out at the Centre for X-ray CT at Ghent University (UGCT). The set-up of the micro-CT scanner was described in detail by Masschaele *et al.* (2007). For the present study, the high power directional head was used as an X-ray source. The samples were scanned at 130 kV with a thin Cu-filter, to minimize beam hardening effects. A total of 800 projections were taken, each projection averaging two frames of 400 millisec exposure time. A Varian 2520V Paxscan (Varian Medical Systems Inc., Palo Alto, CA, USA) was used as an X-ray detector. This detector consists of 1880 × 1496 pixels, with a pixel size of 127 μm × 127 μm. To enhance image statistics, a pixel averaging of 2 × 2 pixels was used which reduced the resolution.

The CT data were processed with the reconstruction software Octopus (UGCT). Three-dimensional morphological analysis was performed using Morpho+ (UGCT). This software enables the volume to be segmented using advanced thresholding techniques (Vlassenbroeck *et al.*, 2007). Furthermore, it allows different objects to be labelled, classified and separated in the volume. VGStudioMax 1·2 (Volume Graphics GmbH, Heidelberg, Germany) from Volume Graphics (64 bit version) was used for 3D volume rendering.

Petrography

Standard thin sections were studied using conventional transmitted, reflected and UV light microscopy. For further investigation of diagenetic features, cold cathode luminescence (CL) was used. Cold CL allows the differentiation of primary biogenic carbonates from diagenetic carbonates and the discrimination of

different cement sequences which formed under changing diagenetic conditions. It is generally accepted that Mn^{2+} and trivalent rare earth element ions are the most important activators of extrinsic CL in carbonate minerals, while ferrous iron (Fe^{2+}) functions as a quencher of CL (Richter *et al.*, 2003). Biogenic carbonate fragments usually are non-luminescent unless they undergo (partial) recrystallization. Diagenetic calcite is typically yellow-orange luminescent, whereas dolomite appears in yellow-red colours.

Individual gypsum crystals were embedded in epoxy. After polishing and carbon-coating, they were studied with a JSM 6400 scanning electron microscope (SEM; JEOL Limited, Tokyo, Japan) at Ghent University. Bulk sediment associated with the gypsum was dissolved in distilled water and treated in an ultrasonic bath for 20 sec. Subsequently, the solution was filtered and dried. The filter was gold-coated and studied with a SEM. The composition of several points was measured using Energy Dispersive Spectroscopy (EDS).

Isotope measurements

The oxygen and sulphur isotopic composition of gypsum-bound sulphate was measured on hand-picked gypsum crystals at the Max Planck Institute for Marine Microbiology Bremen and the Swiss Federal Institute of Technology (ETH) Zurich. The crystals were digested in a $NaCl_2$/ascorbic acid solution and subsequently precipitated in the form of $BaSO_4$ by addition of $BaCl_2$. To determine the sulphur isotopic composition of pyrite, sediment sub-samples were subjected to a two-step chromium-II reduction method (Fossing & Jorgensen, 1989). This method separately traps acid volatile sulphide and chromium-reducible sulphur (CRS) as ZnS. The CRS fraction, which mainly consists of sulphur bound as pyrite, was converted into Ag_2S by treatment with $AgNO_3$. Precipitates were washed several times with deionized water and dried.

Sulphur isotope ratios were measured by adding 0·4 to 0·6 mg of $BaSO_4$ or 0·2 to 0·4 mg Ag_2S to 1 mg of V_2O_5 in a tin capsule and combusted at 1060 °C in an elemental analyser (EURO EA Elemental Analyzer®; HEKAtech GmbH; Wegberg, Germany) to produce SO_2. The evolved SO_2 was carried by a helium stream through a GC column, Finnigan Conflo III®, and into a Finnigan Delta V® (Thermo Fisher Scientific, Waltham, MA, USA) stable isotope ratio mass spectrometer to determine $\delta^{34}S$. The sulphur isotope measurements were calibrated with reference materials National Bureau of Standards (NBS) 127 ($\delta^{34}S = +20{\cdot}3‰$) and IAEA-SO-6 ($\delta^{34}S = -34{\cdot}1‰$). The standard errors ($\sigma 1$) of the measurements were less than 0·2‰ for $\delta^{34}S$.

For oxygen isotope analysis, *ca* 0·16 mg of $BaSO_4$ was transferred to a silver capsule and thermochemically reduced at 1450 °C in the presence of graphite and glassy carbon in the Finnigan Thermal Conversion/Elemental Analyzer (TC/EA®; Thermo Fisher Scientific) to produce CO. The evolved CO was carried by a helium stream through a GC column, Finnigan Conflo III®, and into a Thermo Scientific MAT 253® (Thermo Fisher Scientific) stable isotope ratio mass spectrometer to measure $\delta^{18}O$. The oxygen isotope measurements were calibrated with NBS 127 [$\delta^{18}O = +8{\cdot}6‰$ (Boschetti & Iacumin, 2005)], IAEA-SO-5 ($\delta^{18}O = +12{\cdot}0‰$) and IAEA-SO-6 ($\delta^{18}O = -11{\cdot}3‰$ (Halas *et al.*, 2007)). The standard errors ($\sigma 1$) of the measurements were less than 0·3‰ for $\delta^{18}O$. The isotope measurements are reported with respect to the standards, Vienna Standard Mean Oceanic Water (VSMOW) and Vienna Canyon Diablo Troilite (VCDT).

RESULTS

Core stratigraphy

Based on the magnetic susceptibility, gamma ray density, XRF, XRD and X-ray imagery, core MD01-2459G was subdivided into two units. Unit A comprises the top 535 cm of the core and unit B comprises the lower 544 cm (Fig. 3) (Foubert & Henriet, 2009). Unit A is composed of olive-grey medium-grained silt (5Y 4/2) and contains large coral fragments. In general, the calcium and strontium values are high, but lower than those of unit B. Except for a peak in the top 50 cm, the magnetic susceptibility values of this unit are rather low, averaging around 5 SI. The XRF iron intensities are high compared with unit B, averaging around 12K counts sec^{-1}. X-ray diffraction analysis shows that the sediment matrix of unit A is dominated by quartz (25·6%), calcite (26·7%) and clay minerals (23·7%). Feldspar (7·3%) and aragonite (2·7%) appear in minor quantities (Fig. 4). The age of the corals in unit A have been dated to correspond to the Holocene (Frank *et al.*, in press).

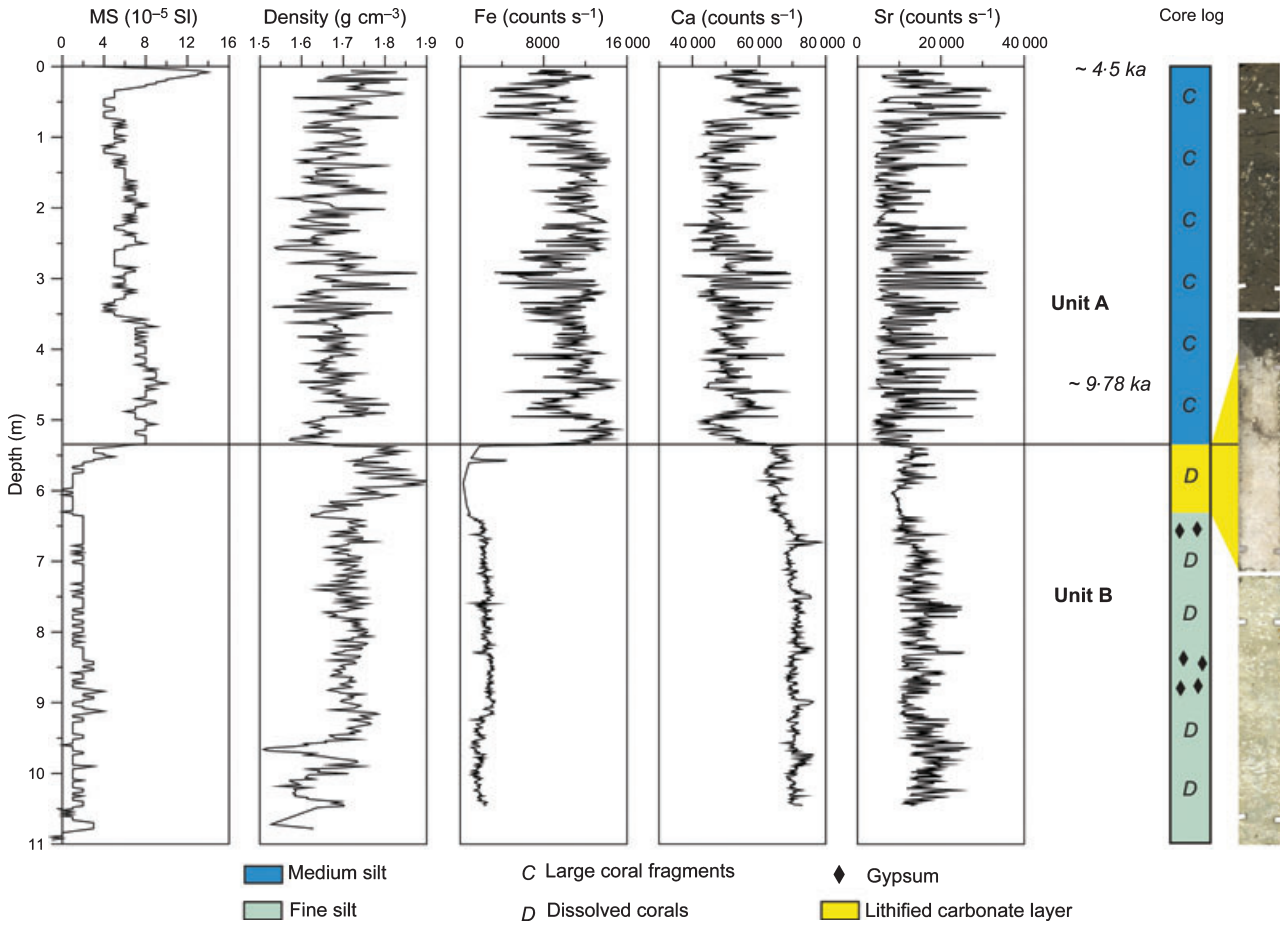

Fig. 3. Overview of the stratigraphy of core MD01-2459G featuring the magnetic susceptibility (MS), density, X-ray fluorescence (XRF), a basic core log. Images of core sections 300 to 375 cm, 525 to 600 cm and 750 to 825 cm are given. U–Th dating of the corals of unit A are also noted (Frank *et al.*, in press). Gypsum crystals were discovered in two intervals in unit B: i.e. at a depth of 658 to 671 cm and 840 to 891 cm (modified after Foubert & Henriet (2009)).

Unit B consists of light-grey fine-grained silt (7.5Y 6/1) rich in diagenetically altered corals which are characterized by fragile skeleton walls. The corals are hardly recognizable on X-ray images, indicating little density contrast between the corals and the surrounding sediment. The alteration of the corals prevented uranium–thorium dating in unit B. The magnetic susceptibility records extremely low values for unit B which can be explained by the presence of carbonate-rich sediments; this is also reflected in the high XRF calcium values, averaging around 70K counts sec^{-1}. The strontium values increase in unit B compared with unit A, while there is a significant decrease in the iron intensities. A remarkable feature in unit B is a lithified carbonate layer between 535 and 630 cm, which is reflected in the high density values. The coral fragments in this layer are (almost) completely dissolved. Between 555 and 560 cm, a horizon of dark, siliciclastic sediment occurs, characterized by a peak in the XRF iron counts. Some lithified carbonate fragments are embedded in the siliciclastic sediment. At 630 cm, there is a sharp boundary to the unlithified sediment below.

X-ray diffraction analysis shows significantly more calcite in unit B than in unit A (Fig. 4). The lithified carbonate layer contains between 68 and 90% calcite with an average of 81%. The sediments of unit B below the lithified layer show lower percentages of calcite, ranging between 55 and 66% (average: 60·1%). The aragonite content of unit B fluctuates strongly. The lithified carbonate layer contains *ca* 5% aragonite while the lower part of unit B contains 8 to 19% aragonite. Quartz (3 to 8%) and clay minerals (3 to 10%) occur in minor abundances. Gypsum, pyrite and

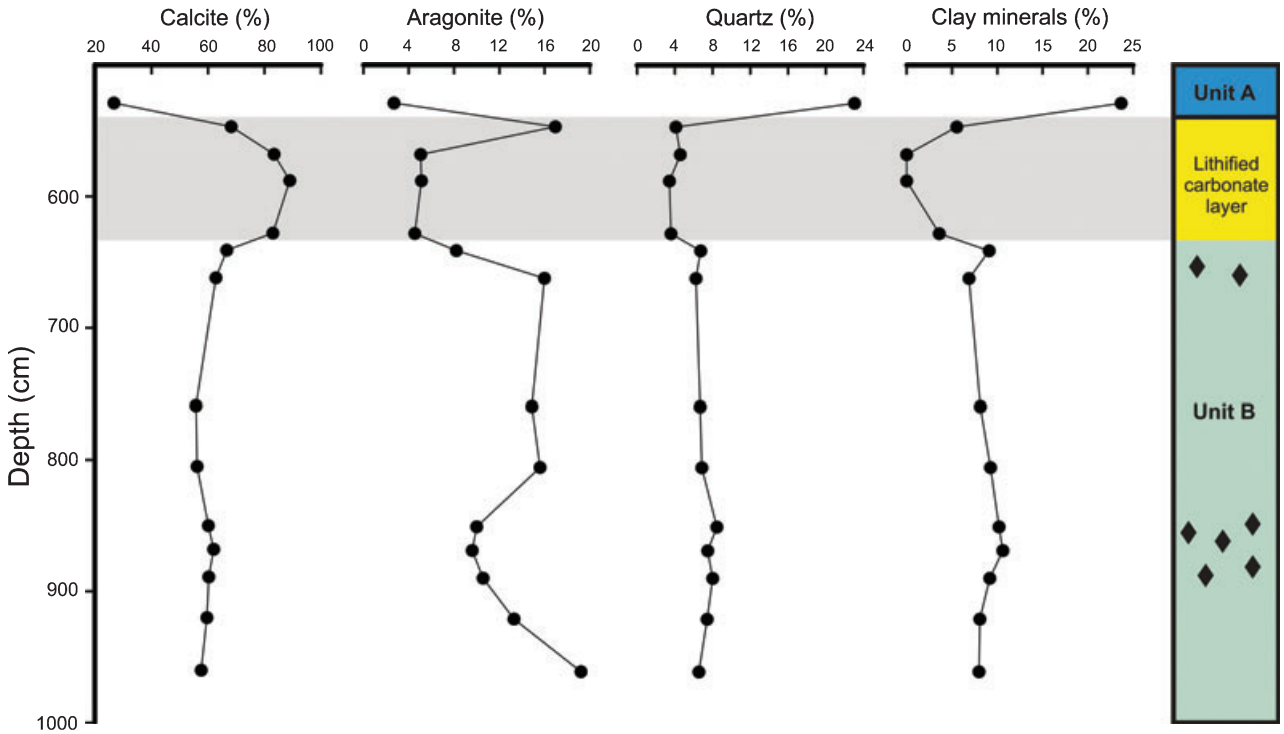

Fig. 4. XRD-data of the bulk sediment. The percentages of calcite, aragonite, quartz and clay minerals are presented.

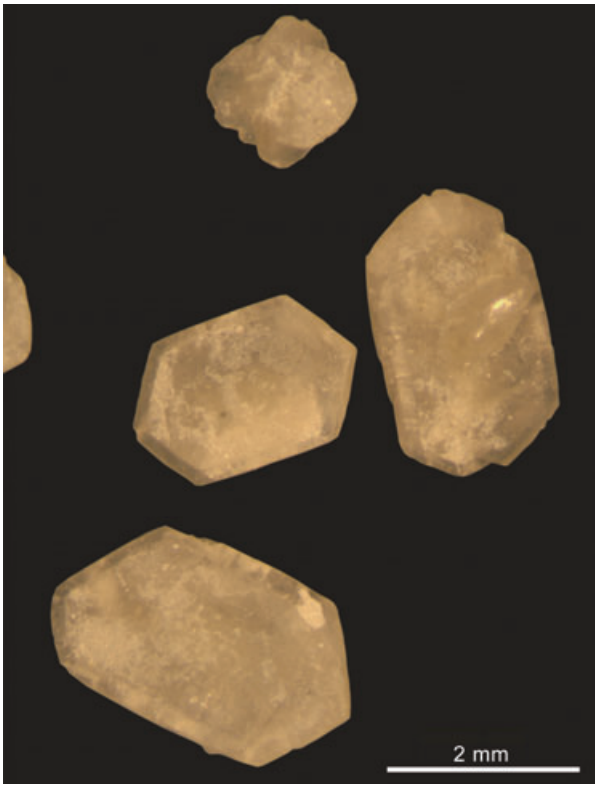

Fig. 5. Euhedral, tabular gypsum crystals with a size between 1·5 and 4 mm. Often, the crystals occur as twins.

dolomite were detected in some samples in very low quantities at the limit of the resolution of XRD analysis (<2%).

Gypsum crystals were discovered in two intervals in unit B: at a depth of 658 to 671 cm and 840 to 891 cm. The gypsum occurs as euhedral, tabular crystals with a size between 1·5 and 4 mm, in a matrix of fine-grained silt. The crystals are transparent white to beige and often twinned (Fig. 5).

Micro-CT scan of unit B

The micro-CT scans enable visualization and quantification of diagenetic features (Fig. 6). Scans of corals from unit B show signs of strong dissolution which created a secondary mouldic porosity (Fig. 6A). Only the most robust parts of the corals, where the septae meet the outer rim of the calyx, are preserved. The scanned sections have a porosity up to 0·43% pores which is almost entirely related to the dissolution of the corals. Micropores could not be visualized in this sample using micro-CT, because the scans were performed with a resolution of 20 μm.

The visualization of the gypsum crystals in unit B clearly shows that the crystals have no preferential orientation and are randomly scattered in

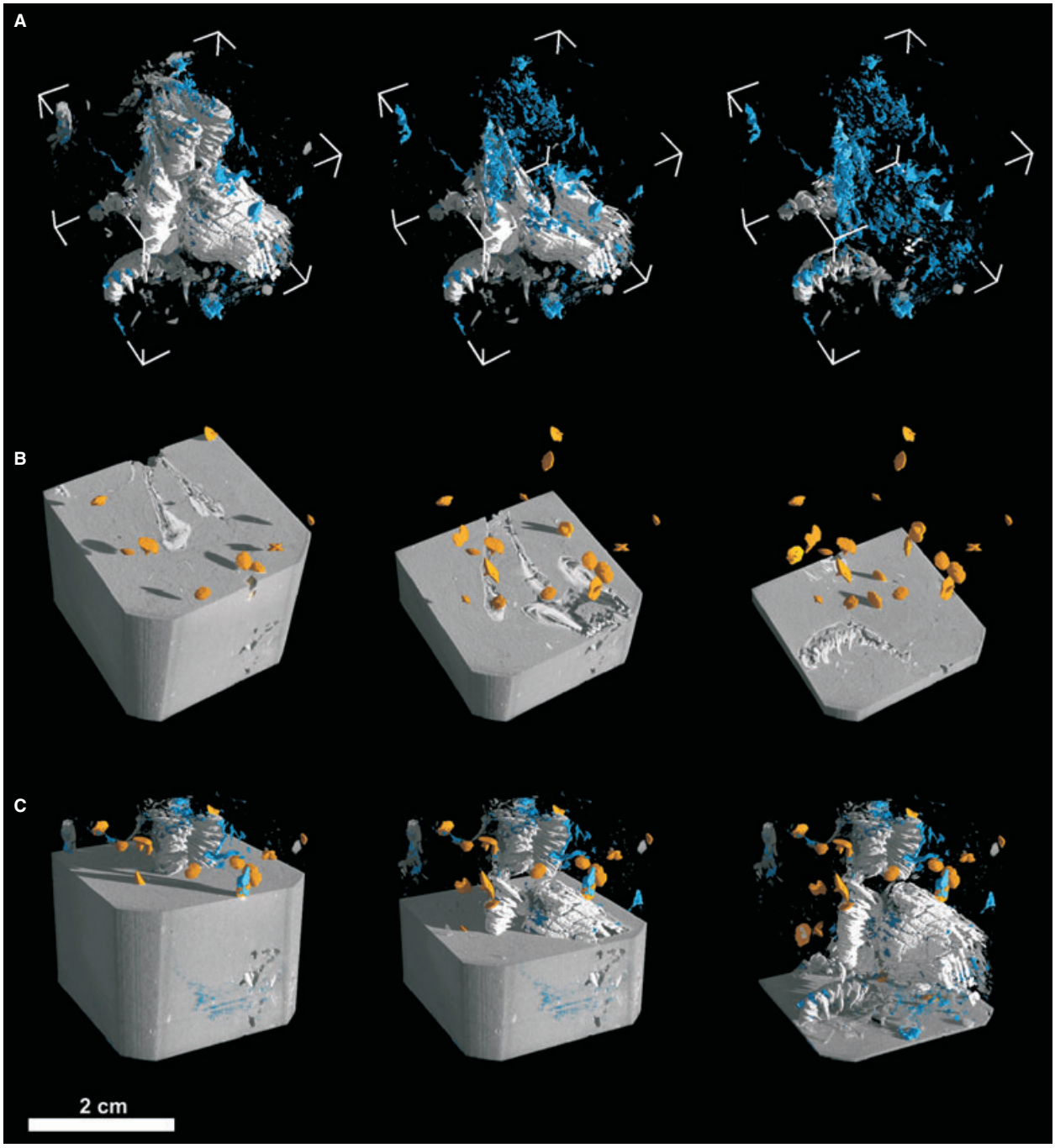

Fig. 6. Micro CT scans of sediment that was sampled at a depth of 889 to 891 cm. (A) Micro-CT scans visualizing the dissolution of the corals (white) and subsequent creation of a secondary porosity (blue). (B) Micro-CT scans showing the occurrence of gypsum crystals (yellow) in the sediment. (C) Overview of the combined occurrence of gypsum (yellow), coral (white) and porosity (blue) in the sediment.

the sediment (Fig. 6B). Quantification of the scans indicates that the samples contain between 0·18 and 0·34 volume % gypsum. There is no apparent spatial correlation between the gypsum crystals and the occurrence of coral relics (Fig. 6C).

Petrography of intervals containing gypsum crystals

The gypsum crystals are embedded in a fine matrix of micritic mud with many biogenic fragments (i.e. corals, foraminifera, bivalve shells,

etc.; Fig. 7A and B). Framboidal pyrite is scattered in the matrix (Fig. 7C). The corals show obvious signs of dissolution whereas the foraminifera are better preserved. Some foraminifera are (partially) filled with the embedding sediment and a few foraminifera contain framboidal pyrite (Fig. 7D).

In two thin sections, faecal pellets were observed in the vicinity of the gypsum crystals, indicating the presence of benthic feeders. There are clusters of framboidal pyrite on the outer rim of the pellets (Fig. 7E).

The gypsum crystals are lens-shaped (Fig. 7A) and often twinned. All crystals contain biogenic fragments such as foraminifera, corals (Fig. 7F) and shell-fragments. Some of the investigated gypsum crystals revealed the presence of framboidal pyrite inside the gypsum (Fig. 7G). A few crystals encase foraminifera containing intraparticular framboidal pyrite (Fig. 7H). These findings were confirmed with SEM-EDS by which calcitic and siliceous biogenic fragments and iron sulphide crystals were identified within the gypsum crystals (Fig. 7I and J). Sometimes, the inclusions in the gypsum are aligned according to the cleavage of the crystals but, in most cases, they appear randomly. A striking feature is the occurrence of broken and even displaced crystals, with displacement occurring along different crystallographic orientations (Fig. 7K). However, it is unclear if this is the result of sample preparation (i.e. sediment sampling, thin section preparation) or a genuine feature.

With the exception of some inclusions, the gypsum crystals are non-luminescent in cold CL. The biogenic fragments are also non-luminescent.

The matrix contains some bright yellow-red luminescent, rhombohedral crystals up to 50 μm with clear zonation (Fig. 7L). These crystals were identified, using SEM-EDS, as dolomite [$CaMg(CO_3)_2$]. The SEM-images reveal the incorporation of coccoliths in the dolomite crystals (Fig. 7M and N).

Isotope measurements

The sulphur isotopic composition of gypsum ($\delta^{34}S$), found at a depth of 890 cm in this core, is +11·0‰ VCDT, the oxygen isotopic composition ($\delta^{18}O$) is +8·9‰ VSMOW. The $\delta^{34}S$ values for pyrite, sampled at different depths, are reported in Table 1.

DISCUSSION

Gypsum and its dehydrated form anhydrite are relatively common in sedimentary deposits throughout the world and throughout the geological record (Bain, 1990). In general, the formation of these gypsum crystals is attributed to evaporation processes, i.e. in hypersaline basins, sabkhas and playas.

An evaporative nature, however, can be excluded for the gypsum crystals in Mound Perseverance. The fact that biogenic fragments and even coral pieces (Fig. 7F) are incorporated into the gypsum indicates that the crystals precipitated *in situ*, due to a diagenetic process. Gypsum occurs only if extraordinarily high sulphate and calcium concentrations cause oversaturation of this mineral. Therefore, reports of non-evaporitic gypsum are limited as this mineral is strongly undersaturated with respect to sea water. Gontharet *et al.* (2007) attributed the precipitation of gypsum in carbonate crusts associated with mud volcanoes to the presence of rising sulphate-rich fluids originating from the dissolution of underlying Messinian evaporites. Gypsum precipitation associated with the formation of sulphate-rich brines in the Bannock Basin was reported by Corselli & Aghib (1987). Bain (1990) attributed the formation of non-evaporitic gypsum to oxidizing calcium-rich groundwater. Similarly, Siesser & Rogers (1976) described gypsum crystals in calcareous plankton-rich sediments on the South West African continental slope in association with authigenic pyrite. The authors propose that pyrite first formed because of the production of sulphide during microbial sulphate reduction which reacted with sedimentary iron phases. Subsequently, a drop in the pH induced the dissolution of calcareous organisms, liberating high concentrations of calcium. Briskin & Schreiber (1978) attributed the occurrence of gypsum in carbonate deep-sea ooze to the influx of oxygen-rich, undersaturated Antarctic Bottom Water, which actively dissolved the foraminiferal ooze, supplying the necessary calcium for gypsum precipitation at the sediment/water interface. Xavier & Klemm (1979) described the occurrence of authigenic gypsum in deep-sea manganese nodules in the Central Pacific Ocean. Wang *et al.* (2004) reported the occurrence of authigenic gypsum crystals associated with gas hydrates at Hydrate Ridge in the Eastern North Pacific. These authors propose that the crystals precipitated at the interface between downward

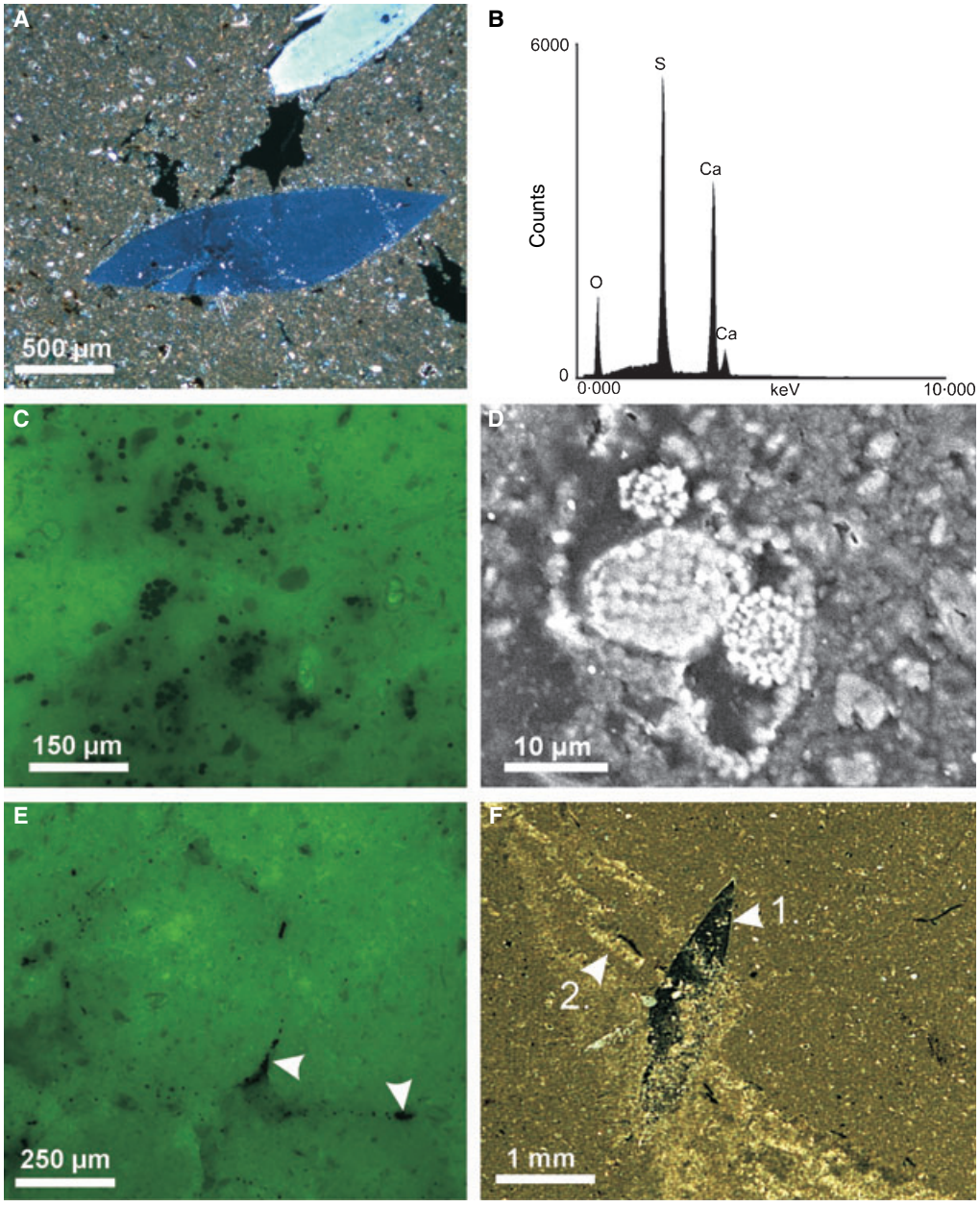

Fig. 7. (A) The occurrence of gypsum crystals in a micritic matrix containing some biogenic fragments (plane-polarized light). (B) An EDS-profile of one of the gypsum crystals. (C) Framboidal pyrite (black spheres) in the sediment associated with the gypsum crystals (UV-light). (D) A detail of a foraminifer containing intraparticular framboidal pyrite (SEM). (E) Clusters of framboidal pyrite on the outer rim of the faecal pellets (UV-light). (F) The incorporation of an altered coral '1' in a gypsum crystal '2' (plane-polarized light). (G) The occurrence of framboidal pyrite '1' incorporated in a gypsum crystal '2' (reflected light). (H) A foraminifer containing intraparticular framboidal pyrite incorporated in a gypsum crystal (reflected light). (I) and (J) SEM images of foraminifera incorporated in gypsum crystals. (K) A twinned gypsum crystal '1' that was broken and displaced in different crystallographic orientations (plane-polarized light). Strongly dissolved coral '2' (L) Cold Cathode Luminescence (CL) of a luminescent dolomite crystal '1' in association with a non-luminescent gypsum crystal '2' and non-luminescent coral '3'. (M) and (N) SEM images of dolomite crystals associated with the gypsum crystals. Note the incorporation of coccoliths into the dolomite crystals in picture (N).

advecting sulphate-rich sea water and gas hydrates, where calcium concentrations are high because of hydrate formation. Similarly, Zhong *et al.* (2007) described the formation of gypsum and pyrite in association with gas venting in the Nansha Trough.

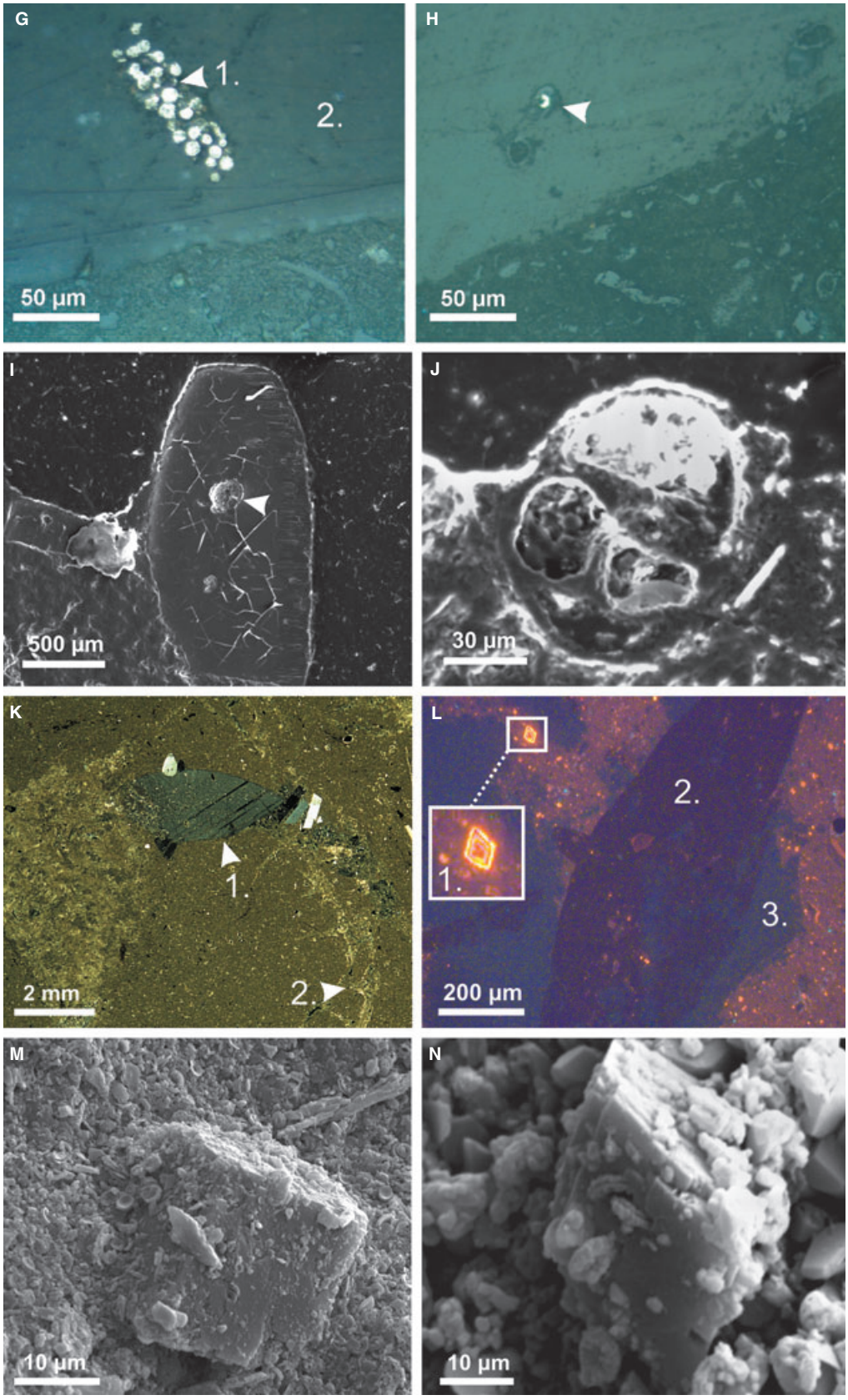

Fig. 7. Continued.

Table 1. Sulphur isotope composition of pyrite occurring adjacent to the gypsum crystals except sample 910 which was sampled in a zone 9 cm below the interval containing gypsum crystals.

Sample depth (cm)	$\delta^{34}S_{pyrite}$ (‰)
870	−22·88
880	−18·89
890	−21·14
900	−17·59
910	−12·30

Gypsum crystals are also sometimes observed on the surface of cores because of the pore water drying-out after core retrieval. In this study, CT scans allowed the amount of gypsum crystals in the matrix to be quantified. Based on a mean value of 0·26 vol%, it was calculated that 33·8 g of gypsum is present in the core in the interval between 840 to 891 cm, using a gypsum-density of 2·3 g cm^{-3}. Gypsum solubility in sea water is up to 3·8 g l^{-1} (Kopittke *et al.*, 2004). Consequently, 8·9 l of sea water would need to evaporate completely to obtain this amount of gypsum. The volume of this core-section is only 8·5 l; therefore, it is impossible to create this quantity of gypsum after coring. Moreover, the core was stored under stable conditions (6 °C), showing no signs of drying out.

To assess the exact timing of gypsum precipitation, uranium–thorium dating was applied to the gypsum crystals. However, the uranium (0·035 p.p.m.) and thorium (0·028 p.p.m.) concentrations in the gypsum are extremely low. Given these low concentrations and the small amount of sample material (0·2 g), the uranium and thorium isotopic values were impossible to determine with sufficient precision. Therefore, the dating of the crystals was not successful.

In this study, the oxygen and sulphur isotopic composition of gypsum and the sulphur isotopic composition of pyrite are used to reconstruct the diagenetic setting during gypsum formation and elucidate the mechanism for the formation of the authigenic gypsum crystals. Based on these findings, a mechanism is proposed that links the formation of gypsum to a phase of increased bottom currents which caused erosion and enhanced inflow of oxidizing fluids into previously anoxic sediments. This process induced the oxidation of pyrite, carbonate dissolution and subsequent gypsum precipitation.

Potential sources of the sulphate in gypsum

The oxygen and sulphur isotopic composition of gypsum can be used to estimate the isotopic composition of the pore-water sulphate from which the gypsum originated. In an open system and at chemical equilibrium, gypsum is enriched in ^{34}S by +1·65‰ and in ^{18}O by +3·5‰ compared with dissolved sulphate (Thode & Monster, 1965; Holser & Kaplan, 1966). However, rapid precipitation of gypsum (i.e. precipitation in disequilibrium) or closed system conditions could suppress this isotope effect. Consequently, the isotopic composition of dissolved pore-water sulphate probably fell between +9·3 and +11·0‰ VCDT for sulphur and +5·4 and +8·9‰ VSMOW for oxygen (Fig. 8, Area B). Compared with sea water sulphate, with a sulphur isotopic composition of +20·3‰ (Longinelli, 1989), the pore-water sulphate from which the gypsum originated was depleted in ^{34}S. Depending on the assumed oxygen isotope fractionation for gypsum precipitation (0 to 3·5‰), the pore-water sulphate had the same oxygen isotopic composition as sea water [8·6‰ VSMOW (Boschetti & Iacumin, 2005)] or was depleted in ^{18}O.

These observations indicate that apart from sea water sulphate, which is a very likely sulphate source for gypsum in marine sediment, another source depleted in ^{34}S relative to sea water sulphate must have contributed to the pore-water sulphate. A potential sulphate source is the oxidation of hydrogen sulphide-rich fluids. At Mound Perseverance, this process is most probably of minor importance. Pore-water profiles from Challenger Mound (IODP expedition 307) located in the close vicinity of Mound Perseverance show no accumulation of hydrogen sulphide within the mound sequence (Ferdelman *et al.*, 2006). Low sulphide concentrations are the result of extremely low rates of anaerobic carbon mineralization (organoclastic sulphate reduction) in cold-water coral bearing sediments (Wehrmann *et al.*, 2009) and a large pool of reactive iron (oxyhydr)oxides that traps sulphide. The oxidation of such accumulated iron sulphide minerals (i.e. pyrite) is the more likely source of sulphate depleted in ^{34}S. Eventually, a mixture of sea water sulphate and sulphate derived from the oxidation of pyrite precipitated as gypsum. This hypothesis is supported by the occurrence of framboidal pyrite within the gypsum crystals in some thin sections which indicates that gypsum precipitated after pyrite formation (Fig. 7G and H).

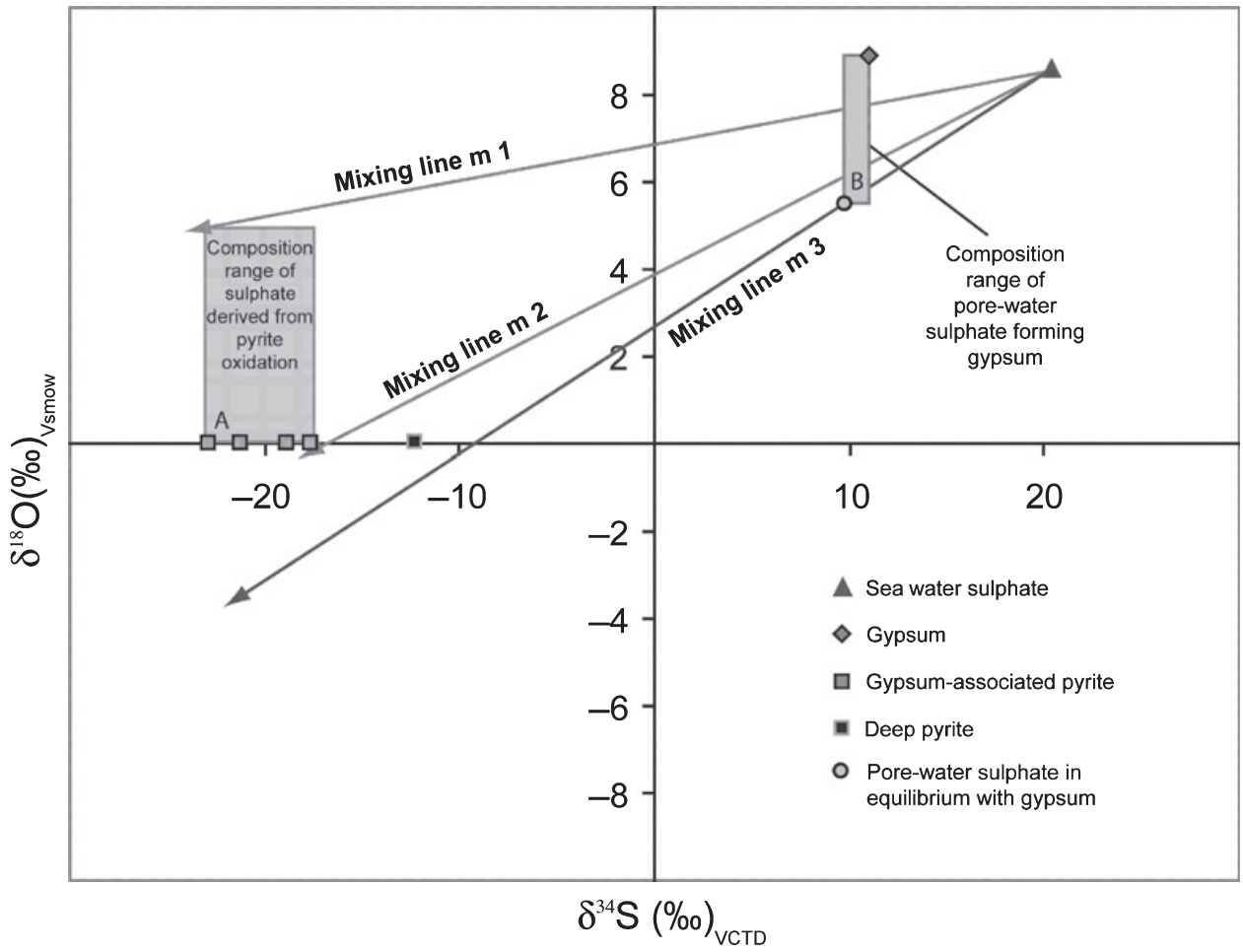

Fig. 8. $\delta^{18}O$ versus $\delta^{34}S$ isotope plot showing the composition for sea water sulphate, gypsum and pyrite.

Estimation of the $\delta^{18}O$ and $\delta^{34}S$ of sulphate derived from pyrite oxidation

Sulphate derived from pyrite oxidation has almost the same sulphur isotopic composition as the original sulphide because sulphur isotope fractionation during this process is smaller than 1‰ (Balci *et al.*, 2007). The sulphur isotopic composition of pyrite within the zone where gypsum was formed varies between −22·9 and −17·9‰. Therefore, it can be assumed that sulphate, derived from partial oxidation of these pyrites, would possess a sulphur isotopic composition covering the same range. The oxygen isotopic composition of sulphate derived from pyrite oxidation depends on the oxygen source (i.e. water and dissolved oxygen) and the oxidation mechanism (Taylor *et al.*, 1984; Toran & Harris, 1989; Balci *et al.*, 2007; Brunner *et al.*, 2008). According to Balci *et al.* (2007), water-derived oxygen accounts for around 90% of oxygen incorporated into sulphate during pyrite oxidation while 10% is derived from dissolved oxygen. Both sources are characterized by very different isotopic compositions: $\delta^{18}O_{H2O} \cong \delta^{18}O_{VSMOW} = 0‰$ for sea water and $\delta^{18}O_{O2} = +23{\cdot}5‰$ for oxygen (Kroopnick & Craig, 1972). In aquatic environments, oxidation of pyrite with oxygen derived from water is associated with a positive oxygen isotope fractionation effect of roughly 0 to 4‰ (Taylor *et al.*, 1984; Balci *et al.*, 2007; Brunner *et al.*, 2008). Oxidation of pyrite with oxygen derived from dissolved oxygen is associated with a negative oxygen isotope fractionation effect of around −10‰ (Kroopnick & Craig, 1972; Balci *et al.*, 2007). Consequently, it can be expected that sulphate derived from pyrite oxidation would have a sulphur isotopic composition of −22·9 to −17·9‰ and an oxygen isotopic composition of 0 to 5‰ (Fig. 8, Area A).

Estimation of the relative contribution of sulphate from pyrite oxidation versus sea water sulphate

Mixing of sulphate from pyrite oxidation with sea water sulphate could have produced the pore-water sulphate which the gypsum precipitated from (Fig. 8). Based on this hypothesis, a sulphur isotope mass balance can be used to assess the contribution of sulphate derived from pyrite oxidation relative to the contribution of sea water sulphate:

$$a \times \delta^{34}S_{pyrite} + b \times \delta^{34}S_{seawater} = (a+b) \times (\delta^{34}S_{gypsum} - \Delta^{34}S_{pore-water\_gypsum}) \quad (1)$$

The parameters a and b denote the contribution of sulphate from pyrite oxidation and sea water sulphate, respectively. $\delta^{34}S_{pyrite}$ denotes the sulphur isotopic composition of sulphate derived from pyrite oxidation and $\delta^{34}S_{sea\ water}$ denotes the sulphur isotopic composition of sea water sulphate. $\delta^{34}S_{gypsum}$ denotes the sulphur isotopic composition of gypsum, and $\Delta^{34}S_{pore\text{-}water\_gypsum}$ the sulphur isotope fractionation for the precipitation of gypsum from pore-water sulphate.

The rearrangement of Eq. 1 allows the introduction of the relative ratio (x), the contribution of sulphate from pyrite oxidation and sulphate from sea water:

$$\begin{aligned}
&a/b \times \delta^{34}S_{pyrite} + \delta^{34}S_{sea-water} \\
&\quad = [(a+b)/b] \times (\delta^{34}S_{gypsum} - \Delta^{34}S_{pore-water_gypsum}) \\
&x \times \delta^{34}S_{pyrite} + \delta^{34}S_{sea-water} \\
&\quad = [x+1] * (\delta^{34}S_{gypsum} - \Delta^{34}S_{pore-water_gypsum}) \\
&x \times [\delta^{34}S_{pyrite} - (\delta^{34}S_{gypsum} - \Delta^{34}S_{pore-water_gypsum})] \\
&\quad = \delta^{34}S_{gypsum} - \Delta^{34}S_{pore-water_gypsum} - \delta^{34}S_{sea-water} \\
&x = (\delta^{34}S_{sea-water} - \delta^{34}S_{gypsum} \\
&\quad + \Delta^{34}S_{pore-water_gypsum})/(\delta^{34}S_{gypsum} \\
&\quad - \Delta^{34}S_{pore-water_gypsum} - \delta^{34}S_{pyrite}) \quad (2)
\end{aligned}$$

The estimates for $\delta^{34}S_{sea\ water}$ (+20·3‰), $\delta^{34}S_{gypsum}$ (+11·0‰), $\Delta^{34}S_{pore\text{-}water\_gypsum}$ (0 to +1·65‰) and $\delta^{34}S_{pyrite}$ (−17·9 to −22·9‰) can be used to calculate the contribution of sulphate from pyrite oxidation relative to the contribution of sea water sulphate. The calculations show that about 22 to 29% of sulphate in gypsum could have been derived from pyrite oxidation. Using the graphical combination of sulphur and oxygen isotope mixing, the relative contribution from pyrite oxidation can be even better constrained. About 23 to 26% of sulphate in gypsum was derived from pyrite oxidation (Fig. 8, mixing lines m 1 and m 2). Assuming that the concentration of sea water sulphate was 28 mM, the calculated values would correspond to a sulphate contribution from sulphide oxidation to the pore-water sulphate pool of 7·7 to 11·2 mM sulphate. To produce the latter amount of sulphate, an oxidation of around 0·1 to 0·2 wt% wet weight pyrite would have been required. Given the amount of pyrite that was observed in the thin-sections (Fig. 7C), this estimate is reasonable.

Two pyrite generations?

The mixing lines in the oxygen–sulphur isotope plot in Fig. 8 do not only allow the calculation of the contribution of sulphate from pyrite oxidation to gypsum (lines m 1 and m 2), but also provide information about the isotope fractionation related to gypsum precipitation. The intercepts between m 1 and m 2, respectively, and the composition range of pore-water sulphate forming gypsum (Fig. 8, Area B) indicate that the isotope fractionation (1·2 to 2·8‰ for $\Delta^{34}S_{pore\text{-}water\_gypsum}$ and 0·6 to 1·2‰ for $\Delta^{18}O_{pore\text{-}water\_gypsum}$) is smaller than the reported equilibrium isotope fractionation [1·65‰ for sulphur and 3·5‰ for oxygen (Holser & Kaplan, 1966; Thode & Monster, 1965)]. Such a suppression of the isotope fractionation effect could be due to closed-system or non-equilibrium conditions, for example, rapid precipitation of gypsum. However, the alternative hypothesis that gypsum formed under isotopic equilibrium, can also be tested. In this case, the sulphur isotopic composition of sulphate derived from pyrite oxidation is estimated using a mixing line through the isotopic composition of sea water sulphate and pore-water sulphate at isotopic equilibrium (Fig. 8, mixing line m 3). It is assumed that the lowest oxygen isotopic composition of sulphate derived from pyrite oxidation is equal to the oxygen isotopic composition of sea water, thus 0‰ VSMOW. Therefore, the sulphur composition of the pyrite that was oxidized would be around −9‰ (intercept of m 3 with $\delta^{18}O_{SMOW}$ = 0‰). This scenario is possible under the assumption that the pyrite associated with gypsum, featuring sulphur isotope values around −20‰ VCDT, formed after gypsum precipitation. In the latter case, an earlier pyrite generation, with sulphur isotope

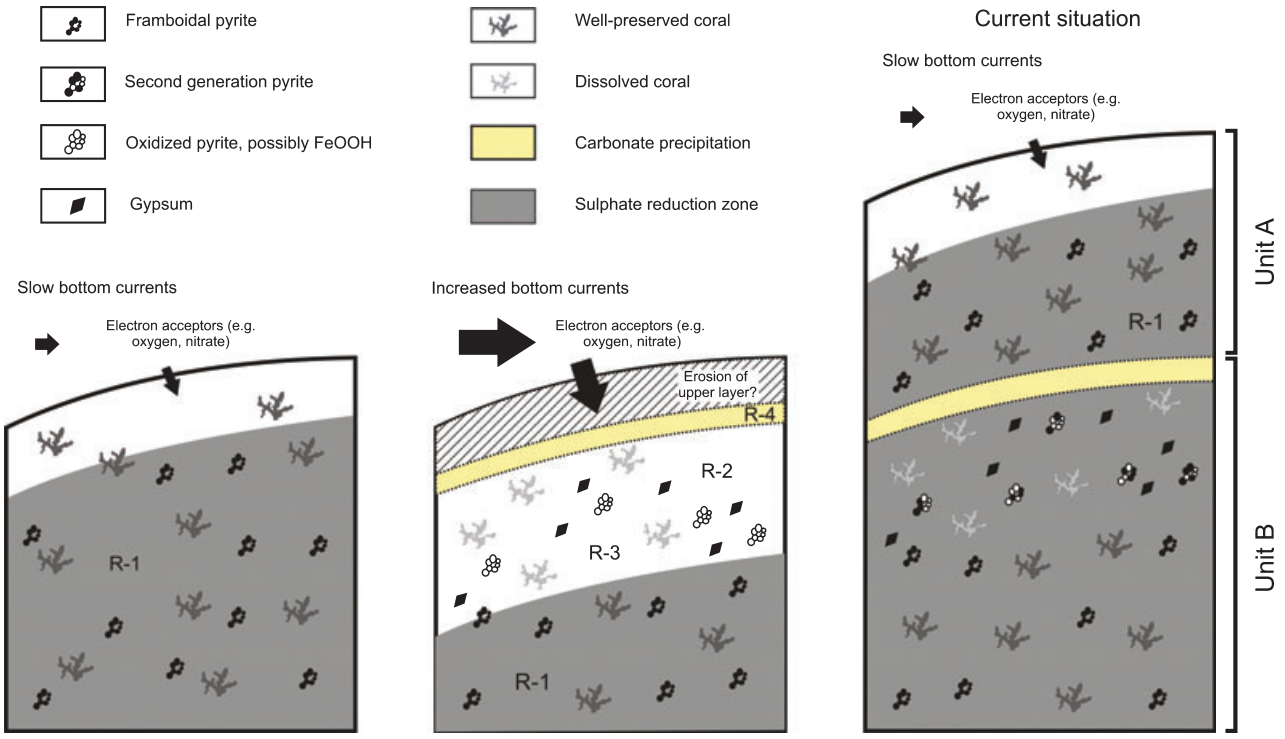

Fig. 9. Schematic representation showing that the increase of bottom current enhances the (sideward) inflow of electron acceptors in the upper layer of the sediment, oxidizing framboidal pyrite. The oxidation of pyrite produces sulphate and acidity, which induces dissolution of aragonitic corals. Subsequently, the produced sulphate and calcium precipitate as gypsum. Erosion of the upper sediment layers, due to the increase of the bottom currents, might have triggered this oxidation process: R-1: formation of framboidal pyrite; R-2: sulphide oxidation buffered by aragonite dissolution; R-3: gypsum precipitation; R-4: precipitation of carbonate near the sea bed.

values around −9‰ VCDT, was to a great extent removed by pyrite oxidation. A sulphur isotopic composition of −12·3‰ VCDT of pyrite found in the layer 10 cm below the zone of gypsum formation supports this hypothesis. Under this assumption (i.e. oxidation of pyrite with $\delta^{34}S$ around −9‰ VCDT), the relative contribution of sulphate from pyrite oxidation would be around 34% (Fig. 8, mixing line m 3).

Proposed mechanism of gypsum and dolomite formation

Initial setting

In marine sediments, oxic to sub-oxic conditions are usually restricted to the top few centimetres while sediments below are anoxic. In cold-water coral bearing sediments anaerobic carbon mineralization is extremely slow (Wehrmann *et al.*, 2009). Sulphate profiles from Challenger Mound suggest decomposition of organic matter by sulphate reduction within the top 50 m of the mound sequence while sulphate reduction coupled to anaerobic oxidation of methane is constrained to the underlying Miocene sediments (Ferdelman *et al.*, 2006). Sulphide produced during sulphate reduction in the mound sediments reacts with ferric iron minerals in the siliciclastic fraction and precipitates as framboidal pyrite (Berner, 1970).

The oxidation event

The oxygen and sulphur isotope values of the gypsum crystals indicate oxidation of pyrite as a driver of the diagenetic alterations in the sediment of Mound Perseverance. It is proposed that oxidizing fluids enter previously anoxic sediments and induce the oxidation of pyrite. Pyrite oxidation with oxygen or ferric iron (Fe^{3+}) as oxidants produces sulphate and protons (H^+) (reactions R-1 and R-2). To maintain reaction R-2, the produced ferrous iron (Fe^{2+}) needs to be oxidized to ferric iron, most probably by oxygen (reaction R-3):

$$FeS_2 + 15/4O_2 + 1/2H_2O \rightarrow Fe^{3+} + 2SO_4^{2-} + H^+ \quad \text{(R-1)}$$

$$FeS_2 + 14Fe^{3+} + 8H_2O \rightarrow 15Fe^{2+} + 2SO_4^{2-} + 16H^+ \quad \text{(R-2)}$$

$$15Fe^{2+} + 15H^+ + 15/4O_2 \rightarrow 15Fe^{3+} + 15/2H_2O \quad \text{(R-3)}$$

Dissolved ferric iron also reacts with H_2O to form iron (oxyhdydr)oxides (reaction R-4):

$$Fe^{3+} + 2H_2O \rightarrow FeOOH + 3H^+ \quad \text{(R-4)}$$

The oxidation event may have been initiated by increasing bottom currents. Van Rooij *et al.* (2007) describe significant variations of bottom currents in the Porcupine Seabight throughout glacial to interglacial cycles. The intensification of the bottom currents enhances the pore-water transport from the bottom water into the sediment, bringing oxidizing fluids into intervals where pyrite previously formed (Fig. 9). This hypothesis is supported by the occurrence of framboidal pyrite within the gypsum (Fig. 7G and H). Increasing currents can induce sediment erosion of a cold-water coral mound (Dorschel *et al.*, 2005), lowering the redox zones in the sediment column. The alternation of reducing and oxidizing conditions might be recorded in the zonation of the dolomites associated with the gypsum crystals (Fig. 7L). The appearance of bright luminescent and non-luminescent layers in the dolomite, points towards crystallization under changing pore-water chemistry conditions (Richter *et al.*, 2003).

The influx of electron acceptors into the upper part of the sediment is favoured by the shape of a mound. This elevated structure promotes lateral inflow of oxidizing fluids. The presence of a coral framework in the mound potentially yields a higher hydraulic conductivity which allows oxidizing sea water to penetrate deep into the sediment. Depreiter (2009) modelled that increased bottom currents will push down the sulphate methane transition zone significantly in an elevated structure on the sea bed, because of the strong lateral inflow of fluids advecting sulphate. Moreover, the organic matter turnover in cold-water coral reef sediments is low because the organic matter is already altered by aerobic and anaerobic microbial-mediated oxidation, leaving very refractory organic material (Wehrmann *et al.*, 2009). This effect also allows a deeper penetration of oxidizing fluids into the mound sediments compared with other surface sediments as oxygen consumption by aerobic carbon mineralization is lower.

Buffering of pyrite oxidation by carbonate dissolution

Pyrite oxidation strongly decreases the pore-water pH. Both oxidation pathways (R1 and R2) produce a similar amount of protons. The production of H^+ (drop in pH) leads to a decrease in the pore-water saturation state for carbonate phases (e.g. high-Mg calcite and aragonite) and hence induces dissolution of these minerals (reaction R-5) (Ku *et al.*, 1999). This process is enhanced by the precipitation of iron oxyhydroxides (R-4):

$$4CaCO_3 + 4H^+ \rightarrow 4Ca^{2+} + 4HCO_3^- \quad \text{(R-5)}$$

This acidification process explains why the coral fragments in unit B are altered significantly, resulting in a secondary porosity (Fig. 6A). In conjunction, XRD-data indicates the preferential dissolution of aragonite in the sediment containing gypsum. The zones of gypsum crystal occurrence are characterized by a decrease of aragonite in the sediment matrix (9·6%), compared with other zones in unit B (below the lithified layer) (average 15·7%), while the calcite content remains stable around 60% (Fig. 4). Brachert & Dullo (2000) and James *et al.* (2005) have already discussed the preferential dissolution of aragonite during early marine diagenesis in cool-water carbonates.

Gypsum formation

The described mechanism of carbonate-buffered pyrite oxidation leads to the addition of dissolved sulphate and calcium; this results in oversaturation of the pore water with respect to gypsum and subsequent gypsum precipitation (reaction R-6):

$$2SO_4^{2-} + 2Ca^{2+} + 4H_2O \rightarrow 2CaSO_4 \cdot 2H_2O \quad \text{(R-6)}$$

The net total reaction of carbonate-buffered pyrite oxidation can be written as follows:

$$\begin{aligned} &FeS_2 + 15/4O_2 + 9/2H_2O \\ &\quad + 4CaCO_3 \rightarrow 4Ca^{2+} + 4HCO_3^- \\ &\quad + 2SO_4^{2-} + FeOOH + 2H_2O \\ &\quad \rightarrow 2CaSO_4 \cdot 2H_2O(s) + 2Ca^{2+} \\ &\quad + 4HCO_3^- + FeOOH \end{aligned} \quad \text{(R-7)}$$

In the following, the mass balance calculation Eq. 2 will be used to test the proposed mechanism under the assumed conditions. The mass balance shows that 23 to 26% (or even 34%) of sulphate in the gypsum crystals derived from pyrite oxidation. For further calculations, a mean value of 25% is used. Assuming a sea water sulphate

concentration of 28 mM, pyrite oxidation contributed 7 mM sulphate. Consequently, the pore-water sulphate concentration during gypsum precipitation is *ca* 35 mM. To produce 7 mM sulphate, an equivalent of 3·5 mM pyrite is oxidized. Oxidation of 3·5 mM pyrite (R-1 and R-2) and subsequent precipitation of iron oxyhydroxides (R-4) result in the production of 14 mM H^+. This reaction is buffered by the dissolution of carbonates (R-4) which produces an equivalent of 14 mM Ca^{2+}. Given that sea water contains 10 mM calcium, the pore-water concentration of calcium during the oxidation event reaches *ca* 24 mM. A sulphate concentration of 35 mM and a calcium concentration of 24 mM results in an ion product of:

$$35 \times 10^{-3} \times 24 \times 10^{-3} = 8{\cdot}4 \times 10^{-4} \text{mol}^2/\text{l}$$

The gypsum solubility product in sea water is in the order of $1{\cdot}52 \times 10^{-3}$ mol^2 l^{-1} (assuming a sea water density of 1030 kg m^{-3}) (Shaffer, 1967) and $4{\cdot}88 \times 10^{-4}$ mol^2 l^{-1} (Kopittke *et al.*, 2004). The calculated value of the ion product of calcium and sulphate is within the range of these values. Thus, gypsum precipitation related to oxidation of pyrite is a feasible process. Gypsum precipitation is even more likely if the possibility is considered that up to 35% of the gypsum may have been derived from pyrite oxidation, which corresponds to an ion product of:

$(1{\cdot}1 \times 10^{-3}$ mol^2 l^{-1} $(37{\cdot}8 \times 10^{-3} \times 29{\cdot}6 \times 10^{-3})$

The calculations show that the concentrations of sulphate and calcium in the pore water must be considerably higher than sea water to reach saturation with respect to gypsum. A semi-closed system is required to allow for the accumulation of calcium and sulphate. Consequently, the oxidant for sulphide oxidation may have been supplied predominantly by diffusive and not advective fluxes.

Dolomite precipitation

Pyrite oxidation and subsequent precipitation of gypsum favours the formation of dolomite (Fig. 7L). The incorporation of coccoliths in the dolomite crystals clearly indicates that these crystals have a diagenetic origin (Fig. 7M and N). Moreira *et al.* (2004) highlighted the role of sulphide oxidation in dolomitization in a lagoon system. The oxidation of sulphide provides acid that decreases the pore-water saturation state for high-magnesium calcite and aragonite, favouring the precipitation of dolomite. Carbonate phases such as calcite and high-magnesium calcite have been found to precipitate competitively with dolomite (Arvidson & Mackenzie, 1999). If auxiliary carbonate phases are prevented from precipitating, dolomite may be the preferred phase. Moreover, the formation of gypsum contributes significantly to dolomitization via incorporation of calcium ions into the gypsum crystals, resulting in an increase of the magnesium/calcium ratio in the associated fluids (Moore, 2001). This process has been described in evaporative marine diagenetic environments (Moore, 2001; Moreira *et al.*, 2004). There are however no reports of a similar process under deep-sea conditions.

Formation of the lithified carbonate layer

In core MD01-2459G, the layer containing gypsum is overlain by a lithified carbonate layer; this suggests a link between the formation of this layer and gypsum precipitation. Most probably, excess calcium and bicarbonate produced during carbonate dissolution diffuse upwards from sites where pyrite oxidation occurs. Close to the sea bed, the pH increases and saturation of the pore water with respect to carbonate occurred which resulted in the precipitation of calcite. The formation of calcite led to the lithification of the sediment at the top of unit B. Usually, the appearance of lithified carbonate layers at the sea bed is associated with increased currents and a reduced sedimentation rate or even erosion (Allouc, 1990; Mutti & Bernoulli, 2003; Noé *et al.*, 2006). This observation supports the hypothesis that erosion, or reduced sedimentation due to increased bottom currents, is responsible for the influx of electron acceptors and subsequent pyrite oxidation in Mound Perseverance.

Return to initial conditions

During the Holocene, unit A is deposited which causes a return to anoxic conditions in the sediments of unit B (Fig. 9). Microbial sulphate reduction recommences, leading to the formation of a second pyrite generation and the removal of the iron oxyhydroxides. The presence of two pyrite generations was already hypothesized, based on the sulphur isotope composition of pyrite in unit B (Table 1).

CONCLUSIONS

In this study, sedimentological, mineralogical and geochemical evidence is presented for a

major diagenetic oxidation event in sediments from a cold-water coral mound. It is hypothesized that increased currents caused partial erosion and enhanced inflow of sea water in the mound; this led to penetration of oxygenated fluids into formerly anoxic sediments. Oxidation of sulphide minerals caused dissolution of aragonite and increased sulphate and calcium concentration, triggering the precipitation of gypsum and dolomite. Near the surface, upward diffusing bicarbonate was reprecipitated as carbonate, leading to a lithification of the sediment. This lithified carbonate layer was buried by Holocene sediments (Fig. 9).

If the hypothesis that increased currents led to an oxidation of anoxic sediments in Mound Perseverance is correct, it can be expected that other cold-water coral mounds in the same region might have undergone similar events of pyrite oxidation. However, layers containing gypsum, that would be diagnostic for such oxidation events, have not been reported in other coral mounds as yet. One possibility is that the oxidation in Perseverance was a local process. The other possibility is that, so far, gypsum crystals went undetected in previous studies. This scenario is likely given that the maximum amount of gypsum found in the gravity core from Mound Perseverance was 0·34 vol%. This quantity is not detectable by X-ray diffraction analysis and is easily overlooked in visual core description. Therefore, it is concluded that the detection of diagenetic gypsum needs to be a target in studies investigating the diagenesis of coral mounds and carbonate sediments in general.

This study demonstrates the importance of environmental factors that affect fluid flow in cold-water coral mounds. It shows how changes in the flow regime impact the (early) diagenesis of these structures. In the future, the occurrence of gypsum in marine sediments could be a powerful tool to identify oxidation processes in carbonate sediments.

ACKNOWLEDGEMENTS

The authors would like to acknowledge the captain, crew and shipboard party of *R/V Marion Dufresne* (2001). The authors express their thanks to J. Moernaut, for his support and many fruitful discussions, S. Glorie, for his help and patience with the SEM-EDS analysis, S.M. Bernasconi for oxygen isotope analysis and B. Bocxlaer for the pictures. Furthermore, the authors would like to thank M. Thierens, B. Neyt, J. Greinert, F. Mees, D. Depreiter, M. Elburg and L. Maignien for their contributions. J. Titschack and one anonymous reviewer provided helpful comments that greatly improved this manuscript. This study was conducted within the framework of the ESF EuroDIVERSITY MiCROSYSTEMS and Genesis (FWO) projects. This research was also supported by the HERMES project, EC contract no. GOCE-CT-2005-511234, funded by the European Commission's Sixth Framework Programme under the priority 'Sustainable Development, Global Change and Ecosystems'.

H. Pirlet is currently funded by the Fund for Scientific Research – Flanders (FWO – Vlaanderen). J. Dewanckele acknowledges the support of the 'Institute for the Promotion of Innovation through Science and Technology in Flanders (IWT-Vlaanderen)'. D. Van Rooij and V. Cnudde are post-doctoral fellows funded by the FWO-Flanders.

REFERENCES

Allouc, J. (1990) Quaternary crusts on slopes of the Mediterranean Sea – a tentative explanation for their genesis. *Mar. Geol.*, **94,** 205–238.

Arvidson, R.S. and **Mackenzie, F.T.** (1999) The dolomite problem: control of precipitation kinetics by temperature and saturation state. *Am. J. Sci.*, **299,** 257–288.

Bain, R.J. (1990) Diagenetic, nonevaporative origin for gypsum. *Geology*, **18,** 447–450.

Balci, N., Shanks, W.C., Mayer, B. and **Mandernack, K.W.** (2007) Oxygen and sulfur isotope systematics of sulfate produced by bacterial and abiotic oxidation of pyrite. *Geochim. Cosmochim. Acta*, **71,** 3796–3811.

Berner, R.A. (1970) Sedimentary pyrite formation. *Am. J. Sci.*, **268,** 1–23.

Boschetti, T. and **Iacumin, P.** (2005) Continuous-flow delta O-18 measurements: new approach to standardization, high-temperature thermodynamic and sulfate analysis. *Rapid Commun. Mass Spectrom.*, **19,** 3007–3014.

Brachert, T.C. and **Dullo, W.C.** (2000) Shallow burial diagenesis of skeletal carbonates: selective loss of aragonite shell material (Miocene to Recent, Queensland Plateau and Queensland Trough, NE Australia) – implications for shallow cool-water carbonates. *Sed. Geol.*, **136,** 169–187.

Briskin, M. and **Schreiber, B.C.** (1978) Authigenic gypsum in marine sediments. *Mar. Geol.*, **28,** 37–49.

Brunner, B., Yu, J.Y., Mielke, R.E., MacAskill, J.A., Madzunkov, S., McGenity, T.J. and **Coleman, M.** (2008) Different isotope and chemical patterns of pyrite oxidation related to lag and exponential growth phases of Acidithiobacillus ferrooxidans reveal a microbial growth strategy. *Earth Planet. Sci. Lett.*, **270,** 63–72.

Corselli, C. and **Aghib, F.S.** (1987) Brine formation and gypsum precipitation in the Bannock Basin, Eastern Mediterranean. *Mar. Geol.*, **75,** 185–199.

De Mol, B., Van Rensbergen, P., Pillen, S., Van Herreweghe, K., Van Rooij, D., McDonnell, A., Huvenne, V., Ivanov, M., Swennen, R. and **Henriet, J.-P.** (2002) Large deep-water coral banks in the Porcupine Basin, southwest of Ireland. *Mar. Geol.*, **188,** 193–231.

Depreiter, D. (2009) *Sources, Modes and Effects of Seabed Fluid Flow*. PhD Thesis, Ghent University, Ghent, 207 pp.

Dorschel, B., Hebbeln, D., Rüggeberg, A., Dullo, C. and **Freiwald, A.** (2005) Growth and erosion of a cold-water coral covered carbonate mound in the Northeast Atlantic during the Late Pleistocene and Holocene. *Earth Planet. Sci. Lett.*, **233,** 33–44.

Ferdelman, T.G., Kano, A., Williams, T. and **the IODP Expedition 307 Scientists** (2006) IODP Expedition 307 drills cold-water coral mound along the Irish continental margin. *Sci. Drill.*, **2,** 11–16.

Fossing, H. and **Jorgensen, B.B.** (1989) Measurement of bacterial sulfate reduction in sediments – evaluation of a single-step chromium reduction method. *Biogeochemistry*, **8,** 205–222.

Foubert, A. and **Henriet, J.P.** (2009) *Nature and Significance of the Recent Carbonate Mound Record: The Mound Challenger Code*. Springer-Verlag, Heidelberg, 350 pp.

Foubert, A., Van Rooij, D., Blamart, D. and **Henriet, J.-P.** (2007) X-ray imagery and physical core logging as a proxy of the content sediment cores in cold-water coral mound provinces: a case study from Porcupine Seabight, SW of Ireland. *Int. J. Earth Sci. (Geol. Rundsch.)*, **96,** 141–158.

Foubert, A., Depreiter, D., Beck, T., Maignien, L., Pannemans, B., Frank, N., Blamart, D. and **Henriet, J.-P.** (2008) Carbonate mounds in a mud volcano province off north-west Morocco: key to processes and controls. *Mar. Geol.*, **248,** 74–96.

Frank, N., Ricard, E., Paque, A., van der Land, C., Colin, C., Blamart, D., Foubert, A., Van Rooij, D., Henriet, J.P., De Haas, H. and **Van Weering, T.** (in press) Carbonate mound evolution on Rockall Bank and in Porcupine Seabight derived from ^{230}Th/U dating of deep-water corals. *Mar. Geol.*

Freiwald, A. and **Roberts, J.M.** (2005) Cold-water corals and ecosystems – preface. In: *Deep-water Corals and Ecosystems* (Eds A. Freiwald and J.M. Roberts), pp. 7–12. Springer-Verlag, Heidelberg.

Gontharet, S., Pierre, C., Blanc-Valleron, M.M., Rouchy, J.M., Fouquet, Y., Bayon, G., Foucher, J.P., Woodside, J. and **Mascle, J.** (2007) Nature and origin of diagenetic carbonate crusts and concretions from mud volcanoes and pockmarks of the Nile deep-sea fan (eastern Mediterranean Sea). *Deep-Sea Res. Part II Topical Stud. Oceanogr.*, **54,** 1292–1311.

Halas, S., Szaran, J., Czarnacki, M. and **Tanweer, A.** (2007) Refinements in BaSO4 to CO2 preparation and delta O-18 calibration of the sulfate reference materials NBS-127, IAEA SO-5 and IAEA SO-6. *Geostand. Geoanal. Res.*, **31,** 61–68.

Hargreaves, P.M. (1984) The Distribution of Decapoda (Crustacea) in the open ocean and near-bottom over an adjacent slope in the northern North-East Atlantic Ocean during Autumn 1979. *J. Mar. Biol. Assoc. UK*, **64,** 829–857.

Henriet, J.-P., De Mol, B., Pillen, S., Vanneste, M., Van Rooij, D., Versteeg, W., Croker, P.F., Shannon, P.M., Unnithan, V., Bouriak, S., Chachkine, P. and **The Porcupine-Belgica 97 Shipboard Party** (1998) Gas hydrate crystals may help build reefs. *Nature*, **391,** 648–649.

Holser, W.T. and **Kaplan, I.R.** (1966) Isotope geochemistry of sedimentary sulfates. *Chem. Geol.*, **1,** 93–135.

Huvenne, V.A.I., Blondel, P. and **Henriet, J.-P.** (2002) Textural analyses of sidescan sonar imagery from two mound provinces in the Porcupine Seabight. *Mar. Geol.*, **189,** 323–341.

Huvenne, V.A.I., Bailey, W.R., Shannon, P.M., Naeth, J., di Primio, R., Henriet, J.-P., Horsfield, B., de Haas, H., Wheeler, A.J. and **Olu-Le Roy, K.** (2007) The Magellan mound province in the Porcupine Basin. *Int. J. Earth Sci. (Geol. Rundsch.)*, **96,** 85–101.

James, N.P., Bone, Y. and **Kyser, T.K.** (2005) Where has all the aragonite gone? – Mineralogy of holocene neritic cool-water carbonates, southern Australia *J. Sed. Res.*, **75,** 454–463.

Jenkins, R. and **De Vries, J.L.** (1970) *Practical X-ray Spectrometry*. MacMillan, London, 190 pp.

Kak, A.C. and **Slaney, M.** (1988) *Principles of Computerized Tomographic Imaging*. IEEE press, New York, 344 pp.

Kano, A., Ferdelman, T.G., Williams, T., Henriet, J.P., Ishikawa, T., Kawagoe, N., Takashima, C., Kakizaki, Y., Abe, K., Sakai, S., Browning, E., Li, X. and **the IODP Expedition 307 Scientists** (2007) Age constraints on the origin and growth history of a deep-water coral mound in northeast Atlantic drilled during Integrated Ocean Drilling Program Expedition 307. *Geology*, **35,** 1051–1054.

Kopittke, P.M., Menzies, N.W. and **Fulton, I.M.** (2004) Gypsum solubility in seawater, and its application to bauxite residue amelioration. *Aust. J. Soil Res.*, **42,** 953–960.

Kroopnick, P. and **Craig, H.** (1972) Atmospheric oxygen – isotopic composition and solubility fractionation. *Science*, **175,** 54–55.

Ku, T.C.W., Walter, L.M., Coleman, M.L., Blake, R.E. and **Martini, A.M.** (1999) Coupling between sulfur recycling and syndepositional carbonate dissolution: evidence from oxygen and sulfur isotope composition of pore-water sulfate, South Florida Platform, USA. *Geochim. Cosmochim. Acta*, **63,** 2529–2546.

Lindberg, B., Berndt, C. and **Mienert, J.** (2007) The Fugloy Reef at 70°N; acoustic signature, geologic, geomorphologic and oceanographic setting. *Int. J. Earth Sci. (Geol. Rundsch.)*, **96,** 201–213.

Longinelli, A. (1989) Oxygen-18 and sulphur-34 in dissolved oceanic sulphate and phosphate. In: *Handbook of Environmental Isotope Geochemistry* (Eds P. Fritz and J.C. Fontes), Vol. 3, pp. 219–255. Elsevier, Amsterdam.

Masschaele, B.C., Cnudde, V., Dierick, M., Jacobs, P., Van Hoorebeke, L. and **Vlassenbroeck, J.** (2007) UGCT: new x-ray radiography and tomography facility. *Nucl. Instrum. Methods Phys. Res., Sect. A*, **580,** 266–269.

Moore, C.H. (2001) *Carbonate Reservoirs: Porosity Evolution and Diagenesis in a Sequence Stratigraphic Framework*. Elsevier, Amsterdam.

Moreira, N.F., Walter, L.M., Vasconcelos, C., McKenzie, J.A. and **McCall, P.J.** (2004) Role of sulfide oxidation in dolomitization: sediment and pore-water geochemistry of a modern hypersaline lagoon system. *Geology*, **32,** 701–704.

Mutti, M. and **Bernoulli, D.** (2003) Early marine lithification and hardground development on a Miocene ramp (Maiella, Italy): key surfaces to track changes in trophic resources in nontropical carbonate settings. *J. Sed. Res.*, **73,** 296–308.

Noé, S., Titschack, J., Freiwald, A. and **Dullo, W.C.** (2006) From sediment to rock: diagenetic processes of hardground formation in deep-water carbonate mounds of the NE Atlantic. *Facies*, **52,** 183–208.

Rice, A.L., Billet, D.S.M., Thurston, M.H. and **Lampitt, R.S.** (1991) The Institute of Oceanographic Sciences Biology programme in the Porcupine Seabight: background and general introduction. *J. Mar. Biol. Assoc. UK*, **71,** 281–310.

Richter, D.K., Gotte, T., Gotze, J. and **Neuser, R.D.** (2003) Progress in application of cathodoluminescence (CL) in sedimentary petrology. *Mineral. Petrol.*, **79,** 127–166.

Richter, T.O., van der Gaast, S., Koster, B., Vaars, A., Gieles, R., de Stigter, H.C., De Haas, H. and **van Weering, T.C.E.** (2006) The Avaatech XRF Core Scanner: technical description and applications to NE Atlantic sediments. In: *New Techniques in Sediment Core Analysis* (Ed. R.G. Rothwell), *Special Publications*, Vol. 267, pp. 39–50. Geological Society, London.

Roberts, J.M., Wheeler, A.J. and **Freiwald, A.** (2006) Reefs of the deep: the biology and geology of cold-water coral ecosystems. *Science*, **312,** 543–547.

Shaffer, L.H. (1967) Solubility of gypsum in sea water and seawater concentrates at temperatures from ambient to 65 degrees C. *J. Chem. Eng. Data*, **12,** 183.

Siesser, W.G. and **Rogers, J.** (1976) Authigenic pyrite and gypsum in South West African continental slope sediments. *Sedimentology*, **23,** 567–577.

Taylor, B.E., Wheeler, M.C. and **Nordstrom, D.K.** (1984) Stable isotope geochemistry of acid mine drainage: experimental oxidation of pyrite. *Geochim. Cosmochim. Acta*, **48,** 2669–2678.

Thode, H.G. and **Monster, J.** (1965) Sulfur-isotopes geochemistry of petroleum, evaporates and ancient seas. In: *Fluids in Subsurface Environments: American Association of Petroleum Geologists Memoir 4* (Eds A. Young and J.S. Galley), pp. 367–377. American Association of Petroleum geologists, Tulsa.

Toran, L. and **Harris, R.F.** (1989) Interpretation of sulfur and oxygen isotopes in biological and abiological sulfide oxidation. *Geochim. Cosmochim. Acta*, **53,** 2341–2348.

Van Rooij, D., Blamart, D. and **Unnithan, V.** (2001) Cruise report MD123-Géosciences: leg 2, part GEOMOUND. RCMG, Gent.

Van Rooij, D., De Mol, B., Huvenne, V., Ivanov, M.K. and **Henriet, J.-P.** (2003) Seismic evidence of current-controlled sedimentation in the Belgica mound province, upper Porcupine slope, southwest of Ireland. *Mar. Geol.*, **195,** 31–53.

Van Rooij, D., Blamart, D., Richter, T.O., Wheeler, A.J., Kozachenko, M. and **Henriet, J.-P.** (2007) Quaternary sediment dynamics in the Belgica mounds province, Porcupine Seabight: ice rafting events and contour current processes. *Int. J. Earth Sci. (Geol. Rundsch.)*, **96,** 121–140.

Vlassenbroeck, J., Dierick, M., Masschaele, B., Cnudde, V., Hoorebeke, L. and **Jacobs, P.** (2007) Software tools for quantification of X-ray microtomography. *Nucl. Instrum. Methods Phys. Res., Sect. A*, **580,** 442–445.

Wang, J.S., Suess, E. and **Rickert, D.** (2004) Authigenic gypsum found in gas hydrate-associated sediments from Hydrate Ridge, the eastern North Pacific. *Sci. China Ser. D Earth Sci.*, **47,** 280–288.

Wehrmann, L.M., Knab, N.J., Pirlet, H., Unnithan, V., Wild, C. and **Ferdelman, T.G.** (2009) Carbon mineralization and carbonate preservation in modern cold-water coral reef sediments on the Norwegian shelf. *Biogeosciences*, **6,** 663–680.

Wheeler, A.J., Beyer, A., Freiwald, A., de Haas, H., Huvenne, V.A.I., Kozachenko, M., Olu-Le Roy, K. and **Opderbecke, J.** (2007) Morphology and environment of cold-water coral carbonate mounds on the NW European margin. *Int. J. Earth Sci. (Geol. Rundsch.)*, **96,** 37–56.

White, M. (2001). *Hydrography and Physical Dynamics at the NE Atlantic Margin that Influence the Deep Water Cold Reef Ecosystem.* Department of Oceanography, NUI, Galway, Ireland.

White, M. (2007) Benthic dynamics at the carbonate mound regions of the Porcupine Sea Bight continental margin. *Int. J. Earth Sci. (Geol. Rundsch.)*, **96,** 1–9.

Xavier, A. and **Klemm, D.D.** (1979) Authigenic gypsum in deep-sea manganese nodules. *Sedimentology*, **26,** 307–310.

Zhong, C., Wen, Y., Mu-hong, C., Jun, L. and **Sen-chang, G.** (2007) Formation of authigenic gypsum and pyrite assemblage and its significance to gas ventings in Nansha Trough, South Chine Sea. *Mar. Geol. Quatern. Geol.*, **27,** 90–100.

Manuscript received 13 March 2009;
revision accepted 30 September 2009